Advanced Materials Interfaces

ADVANCED MATERIALS INTERFACES Open Access

www.advmatinterfaces.de

RESEARCH ARTICLE OPEN ACCESS

Optical Detection and Modeling of Lithium Deposition on Copper Current Collectors

Tjark T. K. Ingber[1] | Len Kimms[2] | Martin Winter[1,3] | Andreas Heuer[2,3] | Diddo Diddens[3]

[1]MEET Battery Research Center, Münster, Germany | [2]Institut für physikalische Chemie, Universität Münster, Münster, Germany | [3]Helmholtz Institute Münster: Ionics in Energy Storage (IMD–4), Forschungszentrum Jülich GmbH, Jülich, Germany

Correspondence: Andreas Heuer (andheuer@uni-muenster.de) | Diddo Diddens (d.diddens@fz-juelich.de)

Received: 20 January 2026 | **Revised:** 22 January 2026 | **Accepted:** 12 February 2026

ABSTRACT

Understanding lithium (Li) deposition on copper (Cu) substrates is essential for improving the performance and lifetime of zero–excess lithium metal batteries. In this study, Li deposition was investigated under realistic coin–cell conditions using complementary scanning electron microscopy and laser scanning microscopy. A semi–automatic image processing workflow enabled quantitative analysis of Li surface coverage and deposit height as functions of current density and deposited charge. Depending on the applied current, Li morphology evolved from isolated hemispherical islands at low current densities to stripe–like structures aligned with the substrate grooves at higher currents. Deposits on rough, dendritic Cu exhibited more compact and vertically oriented morphologies compared to smooth Cu foil. Based on the experimental observations, a phenomenological geometric model was developed to describe Li growth dynamics. The complex transition from isolated island growth to coalesced film formation was captured by a novel combination of a hemispherical growth model and an Avrami–type model with an effective exponent of $n = 1$, which is consistent with numerical simulations. This geometric framework successfully rationalizes the observed dependence of Li morphology and surface coverage on deposition parameters, providing fundamental insights into Li nucleation and growth mechanisms relevant for anode–free battery design.

1 | Introduction

Striving for batteries with a high energy density, scientists have been working on the development of commercially viable long life lithium metal batteries (LMBs) for the past decades. [1–8] Conventionally, the operating principle of such batteries revolves around deposition and dissolution of lithium (Li) at a Li metal negative electrode. However, in the case of Zero–Excess LMBs (ZELMBs) that promise exceptionally high energy density, the Li metal electrode is replaced by a bare current collector acting as the substrate for deposition of Li metal (hereinafter called deposition substrate).[7, 9–15] Between different substrate materials, Li nucleation and growth behavior varies substantially owing to the differences in binding energies, Li surface diffusivities, and deposition and nucleation overpotentials. [13, 16–18] Since inhomogeneous Li deposition and dissolution is a common cause of poor capacity retention and cycle life in ZELMBs, [19–21] investigating the details of the Li deposition behavior on copper (Cu) substrates is very important to improve the electrochemical performance.

Apart from the deposition substrate, the Li morphology substantially depends on the applied current density J that is calculated from the deposition current and the substrate surface area. [22–24] Li deposition at low current densities was reported to produce glassy, amorphous Li nuclei that develop smooth, spherical

Tjark T. K. Ingber and Len Kimms contributed equally to this work.

structures before merging into a uniform Li coating layer on the deposition substrate surface. [25, 26] This is beneficial since the contact area between the deposited Li and the liquid electrolyte is minimized, reducing parasitic reactions that consume both the electrolyte and the limited Li inventory of the battery. [19, 25, 26] In contrast, depositing Li at elevated current densities forms a highly branched network of elongated, crystalline Li whiskers across the deposition substrate surface. [25, 26] This high surface area Li (HSAL) fosters excessive side reactions with the electrolyte, promoting substantial electrolyte decomposition and Li inventory degradation.

The morphology furthermore depends on the employed chemistry of the electrolyte, aging effects of the electrode material like formation of an interphase due to electrolyte decomposition, and construction of the cell so that a wide variety of deposition shapes has been observed elsewhere.[27–29] Here, a commonly used electrolyte composition with a wide stability window is chosen to enable exploration of relevant parameters over a broad range. A recent study by Sun et al. [30] assessed how the Li deposition morphology on Cu and Si substrates is influenced by variation of main deposition parameters like current density J and deposition amount Q, but also applied pressure p and temperature T. The authors evaluated the deposited Li morphology ex situ using scanning electron microscopy (SEM), pointing out different stages of Li surface coverage development while also analyzing the conditions which promote the growth of Li dendrites. The obtained results allowed the identification of multiple successively occurring Li growth modes that describe the deposition process beginning with individual nuclei and resulting in a complete Li coverage of the substrate. Other studies have used operando optical characterization of predominantly dendritic Li deposits through a transparent side window in the cell [27, 29] or a transparent electrode [28]. Yet, these studies were performed either with a modified electrode altering the initial nucleation characteristics, or without a separator neglecting internal pressure effects. However, previous studies have confirmed that the internal cell pressure needs to be considered as it has substantial influence on the Li deposition morphology. [31–33]

The present study provides a detailed investigation of the process of Li deposition on Cu substrates at current parameters commonly used for practical ZELMB operation. Contrasting previous studies, the insights gained here are based on a realistic, widely used coin cell architecture and are applicable to a wide range of current parameters and substrate areas. A standard coin cell architecture was used to ensure that internal pressure conditions are representative of typical applications. Notably, existing hemispherical models [30] are expanded by including parameter regions dominated by complex, overlapping structures of nuclei. The resulting model framework makes extensive use of the Avrami equation [34, 35] and derives corresponding exponents for description. Depending on the applied deposition current, the shape of the Li deposits is found to range from singular islands to a stripe–like morphology that adheres to the native grooves in the Cu substrate surface. This effect is further highlighted in this study by employing a high roughness deposition substrate that is found to promote a substantial difference in Li deposit morphology compared to smooth Cu foil. Thus, the surface structure of the deposition substrate is confirmed as another important parameter guiding the Li morphology, in addition to the deposition current parameters. [36, 37]

Using semi–automatic digital high–throughput SEM image analysis, this work investigates the extent of the Li surface coverage on the Cu substrates, also examining the shapes of the generated Li deposits. Complementing the SEM results, the height profile of the Li deposit structures is analyzed by laser scanning microscopy (LSM). Integrating SEM and LSM results provides a thorough phenomenological understanding of the Li structures generated using different current densities and deposition substrate morphologies. Thus, the integrated approach presented here is sufficient to gain a conclusive understanding while using only widely available microscopy techniques.

Based on the experimental observations, a simple geometrical model is presented which is able to elucidate the dependence of the deposition morphology on the current density and the amount of deposited material. Notably, the fundamental driving factors of the morphology are found to be geometric in nature. This means that a simple hemispherical model is able to capture most of the intricate morphological detail without the added complexity which arise from electrochemical contributions.

The experimental setup, data processing steps, and analysis are discussed in Section 2. Also, an overview of suitable models is given. The results of the surface coverage and deposition height analysis are discussed in Section 3, alongside an interpretation that integrates the experimental findings with insights from modeling. Finally, the main conclusions are summarized in Section 4.

2 | Methodology

2.1 | Experimental

Electrodeposition of Li onto Cu current collectors was performed in coin cells (CR2023) using flat–rolled or dendritic Cu foil as the positive electrode and Li foil (500 μm thickness) as the negative electrode. The separator stack was assembled from two layers of polyolefine nonwoven (Freudenberg FS2190) which were sandwiched between two layers of polypropylene monolayer membranes (Celgard 2500). The separator stack was wetted with 60 μL of a liquid electrolyte formulation that consisted of 1 M Lithium difluoro(oxalato)borate (LidFOB, Sigma–Aldrich) and 0.2 M Lithium tetrafluoroborate ($LiBF_4$, Sigma–Aldrich) in a mixture of diethyl carbonate (DEC, BASF) and fluoroethylene carbonate (FEC, BASF) with a ratio of 2 : 1 by volume as proposed by Weber et al. [31] as a suitable electrolyte composition to promote uniform and reversible Li deposition and dissolution in ZELMBs. Cell assembly was done in an Ar filled glovebox with H_2O and O_2 contents constantly below 1 ppm.

Li electrodeposition using a MACCOR 4000 test system (MACCOR) was conducted in a temperature control chamber (Binder) at 40 °C. After 12 h of resting for uniform electrolyte distribution and temperature homogenization inside the cells, Li amounts of up to 0.75 mAh/cm^2 were galvanostatically deposited onto Cu at currents between 0.1 and 0.5 mA/cm^2. Deposition at an increased current density of 1.0 mA/cm^2 was additionally evaluated for

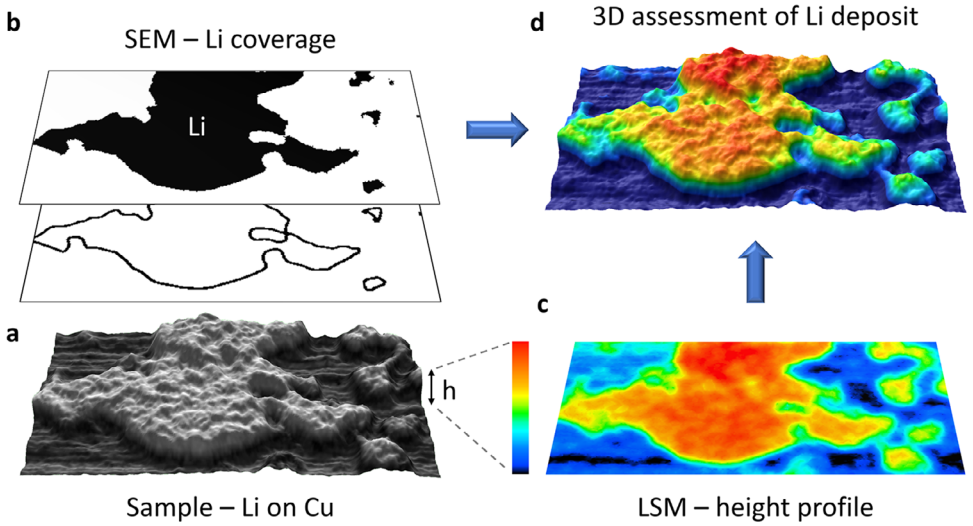

FIGURE 1 | Schematic representation explaining the analysis of (a) Li structures on Cu, combining (b) high–contrast scanning electron microscopy (SEM) imaging for precise differentiation between Li and Cu surfaces with (c) height maps of the Li deposits generated by laser scanning microscopy (LSM) analysis. The results provide (d) full 3D understanding of the sample morphology.

dendritic Cu foil to verify whether the trends identified at lower currents on this substrate would persist under higher current conditions. The deposition amounts Q were adjusted by setting the deposition times t and current densities J at the MACCOR system according to $Q = J \cdot t$. In the inert glovebox atmosphere, a manually operated mechanical pressing device was used to disassemble the coin cells and carefully extract the coated deposition substrates, keeping the deposited Li morphologies intact. Avoiding any exposure to ambient air, the substrates were dried under vacuum before microscopic examination, and any potentially damaged areas were excluded from examination.

SEM images of the prepared samples were acquired using an AURIGA Scanning Electron Microscope (Carl Zeiss Microscopy GmbH) at accelerating voltages between 3 and 10 kV. For each image, acquisition parameters were tuned to provide the highest possible black–white contrast between Cu and Li to optimize the identification of areas covered with Li, while preventing misclassification of regions as black or white and ensuring that no visual distortions occurred.

A VK-H1XMD 3D Laser Scanning Microscope (Keyence) was used to obtain height maps of Li structures on Cu. Inhomogeneities in the Cu deposition substrates were subtracted to obtain an even background for accurate height determination of the Li structures. All presented LSM images use the same color scheme to ensure comparability.

The post–processing steps employed to extract quantitative information use the uncompressed raw data and are described hereafter.

2.2 | Combination of SEM and LSM Imaging

To acquire a full spatial understanding of the Li deposition structures generated herein, integration of different analytical methods is necessary. On the one hand, substrate areas covered in Li (Figure 1a) can be easily differentiated from uncovered Cu using high–contrast SEM (Figure 1b). As a result, the covered surface area can be quantified and intricacies of the deposit boundaries can be observed. However, this method provides only a 2D image that offers limited topographic information and does not allow to quantify the height of the investigated Li structures. This shortcoming is alleviated by integrating complementary LSM height mapping (Figure 1c) that yields accurate 3D positioning data for any point on the investigated sample surface. Yet, LSM alone is insufficient to clearly identify the degree of Li surface coverage as it cannot properly distinguish between Li deposits and inhomogeneities in the Cu substrate that affect the measured height. High–contrast SEM provides a distinct boundary between both regions. Thus, combining the clear boundaries between Cu and Li identified by high contrast SEM with the detailed height information obtained from LSM provides a detailed 3D understanding of the Li deposit morphology on the Cu substrate surface (Figure 1d). This approach exploits the complementarity of the two microscopy methods to expand the level of insight obtained from analyzing the Li deposit morphology. This novel combined method enables a precise understanding about how the variations of different experimental parameters conducted herein affect the Li deposition process.

2.3 | Semi–Automatic Image Processing

SEM and LSM measurements were analyzed employing a semi–automatic post–processing protocol. An overview of the complete image processing from acquisition to analysis is depicted in Figure S1.

The degree of Li surface coverage of the Cu substrate was extracted from the high contrast SEM images. This procedure allows for the rapid distinction between Li deposits and bare substrate. Due to the inherent large–scale heterogeneity of the deposits, analysis of multiple images per parameter set is indispensable. The images per parameter set have been obtained at

different representative locations on the electrode surface and were captured with different magnification to characterize the evolution of the deposition across all relevant length scales. The pixels from the gray–scale SEM images were classified to be either deposited material or substrate based on a threshold value computed using Otsu's method [38]. High–frequent noise was removed first by applying total variation denoising [39]. After the threshold application, jagged edges were smoothed by a Gaussian blur and subsequent reapplication of a binary threshold. The coverage can then be calculated by counting pixels classified as deposits in relation to the image size (Figure 1b).

The LSM measurements contain height data per measurement spot and matching optical pixel values. The electrode was often curved and not level after extraction from the coin cell. In a first post–processing step, the smoothed optical image data was used to identify spots of free Cu substrate. This was done by transforming the pixel color values to the HSV color model, extracting the value component of the resulting image [40], and applying Otsu's method to find a suitable threshold value. The threshold was then used to distinguish areas with deposited Li from regions of bare Cu substrate. Due to the lower contrast as compared to the SEM images, these optical images were not suitable to quantify the coverage. Nonetheless, the image data allowed identification of substrate areas to accommodate automated leveling of the height data. Sufficient free, evenly distributed substrate areas were visible across all evaluated conditions, enabling reliable leveling even at high surface coverage. Leveling was done by fitting a quadratic surface to the complete height data in a first pass and subtracting this curved surface. Next, the fitting was repeated with a subset of the data points identified as substrate by the optical analysis. The subset was collected by discarding the lower 5 % and upper 60 % of selected height data. The discarded data points stemmed from the imperfect detection of substrate in the optical image data and the narrow selection interval was chosen out of an abundance of caution. As large spikes of individual pixels were more prevalent, the upper interval was larger. In a last pass, outliers in the height data were removed by a local Gaussian blur. This procedure provides a height profile of Li deposits on the Cu current collector (Figure 1a,c).

2.4 | Data Analysis and Fitting

Coverage of the Cu current collector was extracted directly from the image processing. Four SEM images of different regions on each electrode surface have been acquired. Images were taken with three different zoom levels of 50, 100, and 200 which were set in the accompanying SEM software. The detection algorithm did not show systematic differences between different zoom levels assuring its robustness. For an improved statistical estimate, the images were divided into four sub–images on which the coverage was evaluated independently. Usually, 48 but no less than 16 data points were evaluated per parameter set. Some images have been discarded because of microscopy artifacts like contrast gradients or chemical residue on the surface.

The volume V of deposited material can be computed by integrating the height data. The underlying LSM data has been acquired at four different regions on the current collector. For comparability, the area independent average deposition height V/A can be calculated by dividing the volume by the measurement area.

Complementary, the height h of the deposition islands can be evaluated as well. The height data captured in a given region on the electrode was further divided into non–overlapping, rectangular subdivisions with $\approx 100\,\mu$m side length. This side length was chosen so that a subdivision always contained substrate and deposits for all samples and was smaller than the large–scale heterogeneity observed for some parameter combinations. The distribution of height values in each subdivision followed a broadened bimodal distribution (see Figure S2). The lower peak was caused by the average height of the substrate in this region and the higher peak indicated the average deposition height. The island height h was calculated as the difference between the two peaks.

2.5 | Li Deposition Modeling

2.5.1 | Hemispherical Model

Experimental studies by Sun et al. [30] have suggested that for low current densities initially distinct islands are formed around nucleation centers. Deposition islands can be approximated as non–overlapping hemispheres placed on the substrate surface, growing unconstrained in all directions equally. The amount of deposited material Q corresponds directly to the volume of the hemispheres. The following geometrical arguments are applicable to other shapes without a preferred growth direction (e.g. pyramides). However, hemispheres and circular shapes respectively allow the simplest description and are therefore commonly used in related literature. [30, 41–43] Deviations from hemispherical growth can be caused by surface imperfections or by space constraints due to the separator in experiments. Notably, contact angles other than 90 ° have not yet been discussed in previous literature, but it is shown herein that the same geometric arguments still hold true.

Previous investigations have shown that Li nucleates instantaneously on Cu substrates because during galvanostatic charging the nucleation overpotential is reached only during an initial short potential peak [44]. Subsequent deposition happens on these initial nuclei and no further nuclei are formed.

Simple geometric arguments show that the island height h (i.e. the radius of a hemisphere) depends on the deposition amount Q as follows (cf. Figure S3 (top)):

$$h \propto Q^{\frac{1}{3}} \tag{1}$$

The surface coverage φ can be computed as the projected circular area on the substrate:

$$\varphi \propto Q^{\frac{2}{3}} \tag{2}$$

In previous experimental studies [30], the island–height growth was constrained by the presence of a separator even before the islands started to coalesce. The complex regime of overlapping neighboring islands was consequently not discussed in previous

studies. If the coalescence begins before any separator effects become governing, a unified growth front develops in the limit of complete coalescence. The substrate surface is covered nearly completely in this limit and the deposition–layer thickness evolves with

$$h \propto Q \tag{3}$$

The transition from the growth of individual islands to film growth cannot be described by this simple model.

2.5.2 | Avrami Model

The transition from randomly distributed islands to complete surface coverage can be elucidated by the Kolmogorov–Johnson–Mehl–Avrami (KJMA) model. [34, 35, 41, 42] A discussion of the derivation and assumptions of this model is given in Section S1. From this point on, the name Avrami model and KJMA model are used synonymously. Assuming randomly distributed seeds and constant island growth, the surface coverage $\varphi(t)$ is given by

$$\varphi(t) = 1 - \exp\left[-S(t)\right] \tag{4}$$

where $S(t)$ denotes the extended surface coverage. [42, 45] The extended surface coverage $S(t)$ is the total surface coverage caused by all islands ignoring overlap, i.e. the sum of the individual base areas of the nuclei. The extended surface coverage S and surface coverage φ are given relative to the total area of observation throughout this work. This value is the same as the observed surface coverage ($\varphi = S$) for isolated islands but becomes larger than the surface coverage ($\varphi < S$) if islands overlap. The overlap effectively leads to a loss in observed covered surface area and, consequently, in deposition volume relative to the values for spatially separated, non–overlapping nuclei. Generally, the extended surface coverage can be expressed as $S(t) = \hat{k}t^n$ where $\hat{k}$ is a proportionality constant and n is referred to as Avrami exponent [42].

Assuming a constant deposition rate, the time dependence can be transformed into a Q–dependence by $t \propto Q$. The surface coverage can be expressed as

$$\varphi(Q) = 1 - \exp\left[-kQ^n\right] \tag{5}$$

in such cases where k is a proportionality constant different to $\hat{k}$. The Avrami exponent derived from the geometric arguments presented by the hemispherical model is $n = \frac{2}{3}$. This however does not account for the intricate effects caused by the overlap of neighboring islands which change the value of n for constant–current conditions. The results discussed later in this paper suggest that an effective Avrami exponent of $n = 1$ may better suited to describe the island growth with instantaneous nucleation and a constant growth rate.

2.5.3 | Numerical model

In order to get a better understanding of the deposition mechanism, a very simple numerical 3D model has been devised. This model aims to recover the fundamental relations involved in the formation of the structured surface coverage by focusing on geometric effects only and neglecting the intricacies of the electrochemical interplay between substrate and electrolyte. Importantly, this model captures the full growth regime, starting from individual islands, progressing to complex overlapping structures, and converging to the limit of a unified growth front.

On a 2D substrate plane with area A, a given number n_{seeds} of initial nucleation centers can be randomly placed in continuous space. Periodic boundary conditions were applied in the lateral directions in order to approximate an infinitely large substrate surface and avoid artifacts caused by an aperiodic boundary. The approximation of a system without boundary effects was necessary because the experimentally observed snapshots of the electrode were far away from the substrate edge. Further implementation details are elaborated in Section S2.1. From the initial germs, hemispheres with a given radius r grew on the surface (see Figure S5). The radius was systematically sampled within a predefined interval $r \in [0, r_{\max}]$. For any given r, the extended surface coverage $S(r)$ is trivially given by

$$S(r) = \frac{n_{\text{seeds}}}{A} \cdot \pi r^2 \tag{6}$$

The total extended volume $V_{\text{ext}}(r)$ is easily accessible as well:

$$V_{\text{ext}}(r) = n_{\text{seeds}} \cdot \frac{2}{3}\pi r^3 \tag{7}$$

By numerical integration, the effective volume $V_{\text{eff}}(r)$ of the total deposits formed by all hemispheres can be computed. Similarly, the surface coverage φ can be numerically determined by projecting the hemispheres onto the substrate. The effective volume is always $V_{\text{eff}} \leq V_{\text{ext}}$ because any overlap reduces the effective volume compared to the extended volume. The same relation applies for the relation between the surface coverage φ and the extended surface coverage S. It should be noted that the volumes are determined in absolute terms and the areas are calculated in relation to the substrate area to give the coverage. This model can be connected to the experimental data by identifying

$$Q \equiv V_{\text{eff}} \tag{8}$$

The effective volume

$$V_{\text{eff}}(r) \propto r^l \tag{9}$$

inherently depends non–linearly on the radius r of the spherical deposits through the empirical exponent l. In contrast, the experimental quantity $Q(t)$ depends linearly on the time of Li deposition given the constant deposition rate and can be used as a suitable proxy of the timescale. The experimental timescale can be connected to the radius r in the numerical simulations by using Equation (8) which in turn enables the comparison of all radius–dependent observables of the simulation to the experimental data. The Avrami exponent n can be readily expressed as

$$n = \frac{2}{l} \tag{10}$$

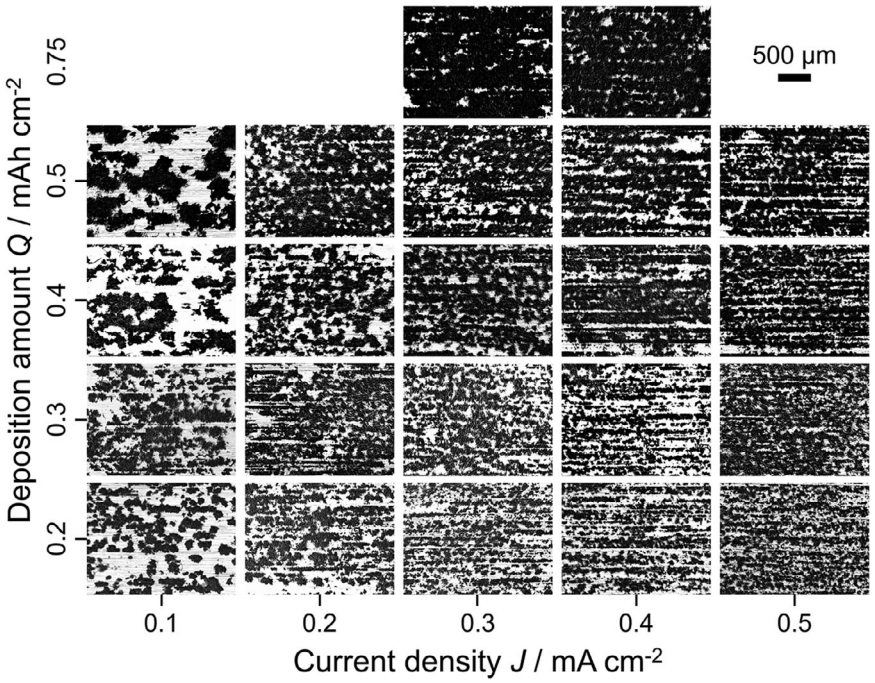

FIGURE 2 | Li structures (black) on pristine Cu foil (white) resulting from electrodeposition of Li amounts Q ranging from 0.2 to 0.75 mAhcm^2 at current density values J from 0.1 up to 0.5 mAcm^2 at 40 °C. High–contrast SEM images acquired at 200× magnification.

by inserting Equation (9) into Equation (6) and identifying the exponent n in the Avrami Equation (5). This connection is used later in this work to interpret the observations.

Furthermore, a generalized dependence between the experimental quantities of surface coverage and volume was discovered by modeling in Section S2.6. An Avrami exponent $n = 1$ is generally suitable using assumptions detailed in Section S2.6.2. Different contact angles $\alpha \neq 90°$ can be investigated by placing spherical caps on the substrate surface. As discussed in Section S2.2, the contact angle does not change the qualitative behavior.

3 | Results and Discussion

3.1 | Li Surface Coverage

The present study focuses on examining Li structures formed under deposition current conditions that are likely to occur in practical battery cells to maximize the applicability of the obtained results. High–contrast SEM images of Li structures generated by electrodepositing Li amounts Q between 0.2 and 0.75 mAhcm^2 onto flat Cu foil at current densities J ranging from 0.1 to 0.5 mAcm^2 are presented in Figure 2. Deposition at $J = 0.1$ mAcm^2 produced rounded, medium–sized Li islands that occasionally converged to form small cluster structures. These islands were slightly oriented along the native groove pattern in the deposition substrate surface, yet this influence was limited as islands extending perpendicular to the grooves were also present. The primary Li deposition islands shrank and gained a more fissured and curved appearance when J was elevated, increasingly coalescing into a stripe pattern along the grooves in the deposition substrate (cf. Figure S17). This advancing stripe geometry dominated the Li deposit morphology at $J > 0.3$ mAcm^2, at the same time reducing and separating the remaining areas of uncovered Cu.

Figure 2 shows changes in the shape of the Li deposits and the extent of the covered area when deposition current conditions were varied, indicating a transition between two distinct growth modes as a function of the deposition current density on flat substrate. Li structures expanded uniformly around the initial Li nucleus at $J = 0.1$ mAcm^2, growing with little regard to the surface texture of the deposition substrate. This implies a thermodynamic regulation of the Li deposition process and negligible concentration gradients at low J values that promote energetically favorable deposition patterns, producing the mentioned island–like Li morphology and limited agglomerations where the Li islands were close together. The spherical island shape may be favorable because it minimizes the interaction energy with the lithiophobic Cu substrate. When J was elevated, the Li deposition seemed to get more oriented along the grooved texture of the deposition substrate (cf. pristine Cu in Figure S23a), resulting in an increasingly stripe–like deposition morphology. The stripes were commonly tens of micrometers wide and up to several millimeters long. This anisotropic growth along one preferred direction was coupled with smaller individual deposit diameters and increased curvature and complexity of the individual deposit borders as indicated by visual inspection. A smaller individual deposition diameter matches an expected increase of initial nucleation centers. These changes together indicate a more fine–grained and less dense deposition morphology that resulted in increasing Li surface coverage at rising J. These observations imply that the Li growth mode at high J was controlled by the Li^+ diffusion kinetics in the electrolyte which can create local concentration gradients. Cation depletion near the surface fostered

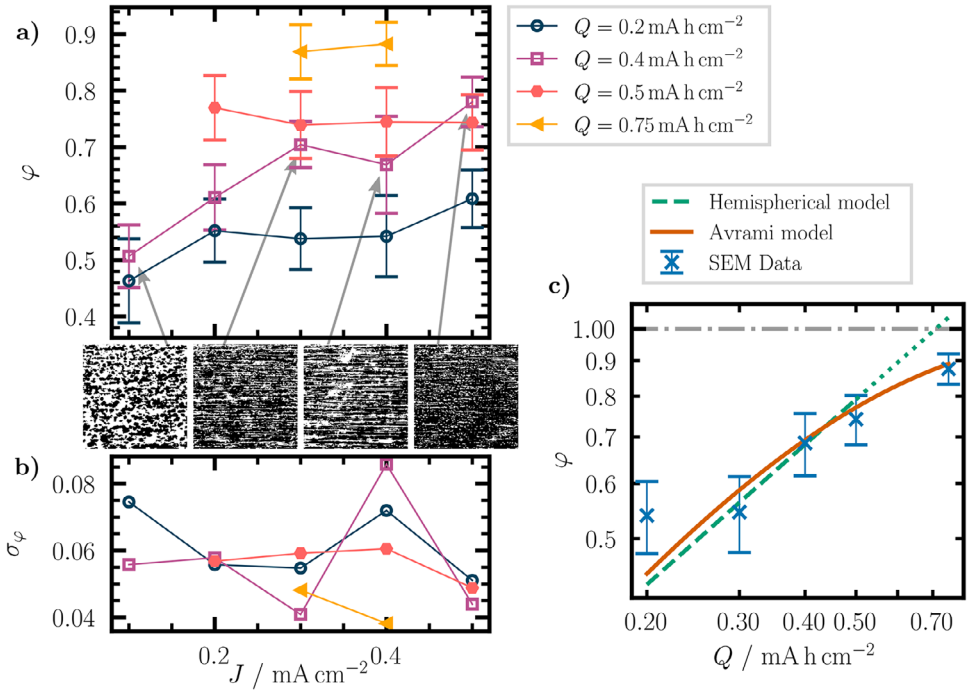

FIGURE 3 | (a) Surface coverage and (b) spatial standard deviation of the surface coverage with varying J. Filled symbols indicate nearly complete coverage for all values of J. Binary SEM images of Li (black) on Cu substrate (white) are added for $Q = 0.4\,\mathrm{mAhcm^2}$ and exemplary current densities J. (c) Surface coverage with varying Q. Values are averaged over all J. Complete coverage is indicated at $\varphi = 1$ and two model predictions are drawn.

deposition along the locally protruding substrate grooves instead of formation of the most energetically favorable Li morphology. Also, metal particles may not have had enough time to rearrange locally to form a smooth surface before subsequent deposition reactions took place. Visual inspections of the SEM images indicated a transition between thermodynamic and kinetic deposition control which took place around $J = 0.3\,\mathrm{mAcm^2}$, resulting in a transitional morphology that represented a mixture of islands and stripe shapes.

A quantitative analysis of the surface coverage augmenting the previous visual analysis is shown in Figure 3a. The observed morphological transition was evident in this analysis as well. For high capacities $Q \geq 0.5\,\mathrm{mAhcm^2}$, the surface was covered to a large degree and the dependence on the current density was not discernible. However, the coverage generally increased with an increase in current density for lower capacities. Interestingly, this behavior was less clearly pronounced for a current density of $J = 0.4\,\mathrm{mAcm^2}$.

Notably, this anomaly in the surface coverage coincided with an increased variance between different measurements for a current density of $J = 0.4\,\mathrm{mAcm^2}$ as depicted in Figure 3b. At this critical current density, there was measurably a higher macroscopic variance between different regions on the current collector. The shown binary SEM images supported the observed spatial variance. Anomalously high variance when reaching high surface coverage was reproducible across different batches (cf. Figure S26) and can be emulated by the geometric model (cf. Section S2.4).

The mentioned transition of the Li growth mode from island–like to stripe–like morphology was observable throughout the range of applied Q values (cf. Figure 2). At growing Q, the amount of deposited Li gradually increased, which caused the deposited Li structures to grow laterally and converge with each other. As a result, the Cu surface was increasingly covered with a continuous Li layer (especially at high J values), and the uncovered Cu areas decreased progressively. Yet, the rate of Li surface coverage growth was reduced at higher Q, indicating a transition from horizontal to vertical expansion when there was not enough free Cu surface left around the Li deposits to accommodate further lateral growth.

The amount of deposited Li metal was systematically varied so that a range between low coverage and the limit approaching full coverage was investigated. Again, the full range of experimental observations was analyzed quantitatively by image processing to augment the visual inspection. The ratio of covered surface (φ) was extracted from the SEM images and plotted in Figure 3c. For low capacities Q, the surface was covered with partially overlapping islands of Li metal which increasingly coalesced for larger Q. Island nucleation was dependent on the surface texture as the Li deposits follow the grooved surface. This matches previous observations [30] showing that the formation of Li islands followed the Cu surface texture. Furthermore, the same stripe–like deposition has been previously attributed to the use of rolled copper substrate in [46]. The surface coverage naturally increased with Q and converged against full coverage. But, the hemispherical model described the presented data well for $\varphi < 85\%$ only. The deviation for high surface coverage was caused by the increased likelihood of overlap between neighboring islands at these conditions. A description of the complete growth phase is given by the Avrami model with an exponent $n = 1$ (cf. also Figure S25).

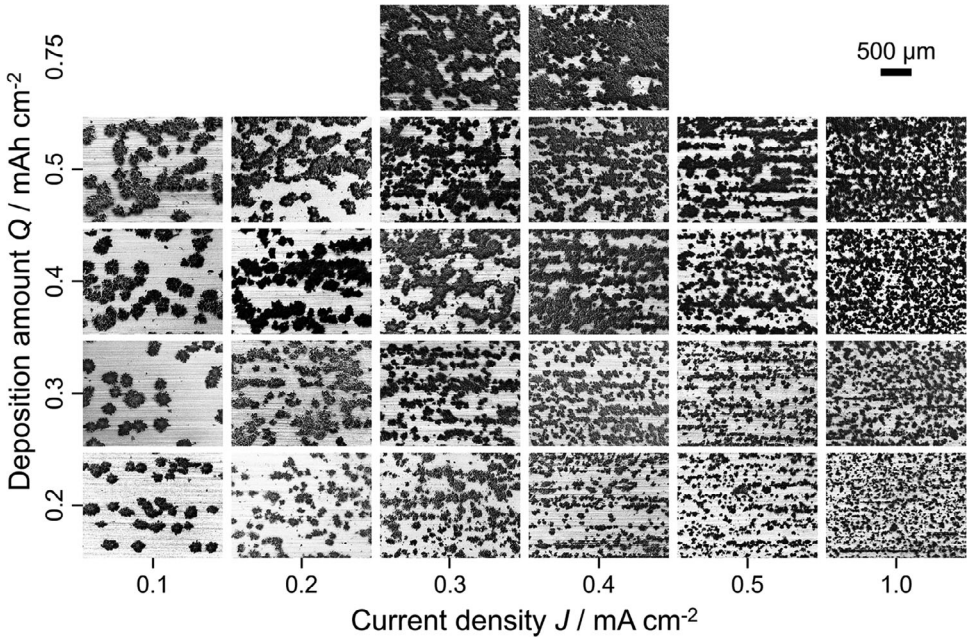

FIGURE 4 | Li structures (black) on dendritic Cu foil (white) resulting from electrodeposition of Li amounts Q ranging from 0.2 mAhcm^2 to 0.75 mAhcm^2 at current density values J from 0.1 mAcm^2 up to 1.0 mAcm^2 at 40 °C. High–contrast SEM images acquired at 200× magnification.

As an example for the experimental timescales involved, estimates of the deposition time were done for a median current density. Half the surface was roughly covered after approximately 45 min of deposition at $Q \approx 0.23$ mAhcm^2 for a median current density of $J = 0.3$ mAcm^2 (cf. Figure 3c). Complete coverage is expected to be reached after seven times this duration (see argumentation in Section S2.6.1), or approximately three and a half hours of deposition at $Q \approx 1.61$ mAhcm^2, which is outside the investigated range. The exact duration depends directly on the rate J of course.

To assess the impact of the deposition substrate roughness and to compare the generated deposits to those on flat Cu foil, Li was electrodeposited onto dendritic Cu foil that had a substantial surface roughness. This substrate had randomly distributed dendritic Cu structures, typically several hundred nm thick and spaced up to 500 nm apart (see Figure S23b). LSM analysis revealed Cu dendrite heights of up to 2 µm so that the dendrites are the dominant microstructural feature of the substrate material. High–contrast SEM images in Figure 4 depict Li structures on dendritic Cu formed by depositing Li amounts Q from 0.2 to 0.75 mAhcm^2 at a current density range J between 0.1 and 1.0 mAcm^2. Throughout the investigated parameter range, the Li morphology on the rough substrate was always based on individual island–shaped deposits without a dominating stripe pattern, contrary to the observations for flat Cu foil. On the dendritic substrate, Li generally deposited in a smaller number of larger individual structures that showed reduced coalescence compared to flat Cu foil. While progressing Li deposition at elevated Q values led to expansion and merging of the Li islands, the overall surface coverage generally remained lower than the coverage observed on flat Cu foil at the same deposition parameters. Even at the largest investigated deposition amount (0.75 mAhcm^2), substantial areas of uncovered Cu remained between the Li deposits, in contrast to the fairly uniform Li layer formed across the flat Cu foil. Higher Q values typically resulted in larger Li islands, while deposition at increasing J generated smaller but more numerous islands. Therefore, the largest islands were deposited at high Q and low J, and the smallest structures were found at the opposite conditions. Enhancing the deposition amount led to increased Li island convergence, while increasing J slightly reduced this tendency. As a result, Li deposition on dendritic Cu foil produced a mostly isotropic, speckled pattern of periodically alternating Cu and Li that became increasingly fine–grained at growing J. The reduced surface coverage compared to flat Cu foil was due to a more compact Li deposition morphology on dendritic Cu as well as a preference for height growth instead of horizontal expansion.

The difference between the Li deposition patterns on flat and dendritic Cu foil implies that, in addition to the current density, the substrate surface roughness also had a substantial impact on the morphology of electrodeposited Li. This was likely caused by the wider current density distribution on dendritic Cu foil due to the increased surface area, which resulted in lower local current densities at the dendrite tips, fostering denser Li deposition.[9] High–magnification SEM images in Figure S24 confirmed that Li deposition onto dendritic Cu foil generated a denser Li morphology with reduced surface area as compared to flat Cu foil. Moreover, the gap between individual dendrites likely hindered the diffusion of Li along the Cu surface during the deposition process, thus preventing a spreading of Li across the dendritic Cu foil. Instead, direction of Li diffusion toward existing Li structures led to accumulation of Li at these sites, fostering continuous growth of fewer separated Li islands. Also, the mentioned gaps between the Cu dendrites promoted vertical growth of Li islands instead of lateral expansion, contributing to the limited Li surface coverage on dendritic Cu foil. The increased surface roughness may also have aggravated the lithiophobicity to the Cu substrate.

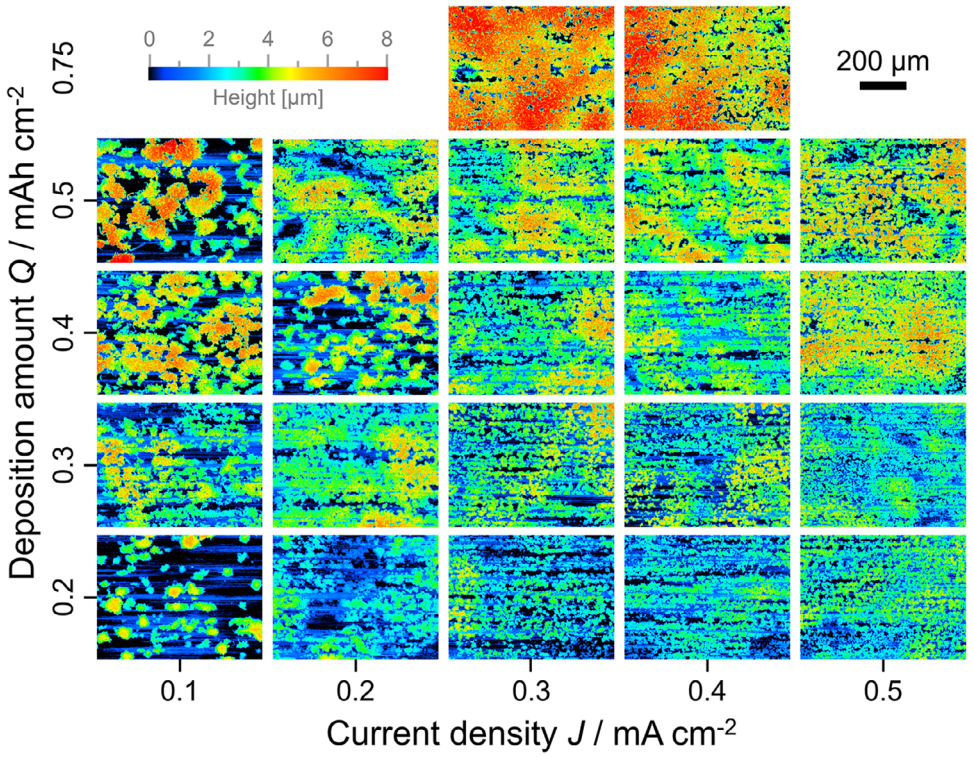

FIGURE 5 | Height maps of Li structures representing deposition amounts Q from 0.2 to 0.75 mAhcm^2 electrodeposited onto flat Cu foil using current density values J ranging from 0.1 to 0.5 mAcm^2. LSM images acquired using 20× lens magnification.

3.2 | Deposition Height

The LSM images in Figure 5 show height maps of Li structures representing deposition amounts Q between 0.2 and 0.75 mAhcm^2 that were electrodeposited on flat Cu substrate using current densities J ranging from 0.1 to 0.5 mAcm^2. The images generally confirm that enhancing the deposition amount Q fostered continued deposit growth, increasing the overall height of the Li structures on the Cu foil. Moreover, the height growth was accelerated at higher Li surface coverage due to limited free space around individual Li deposits, inhibiting lateral expansion. Yet, the deposit height showed regional differences across the sample surface, which implies local variations in Li deposition rates. This was likely due to regionally differing Li^+ influx caused by locally inhomogeneous Li dissolution and transport at the surface of the counter electrode and surface defects on the characterized Cu electrode. Also, Li^+ transfer between the electrodes might have shown regional variations because of local inhomogeneities of the Li metal counter electrode and the separator stack. Furthermore, protruding Li structures were reported to influence the electric field around them, attracting further Li deposition to their location. [47–49] This may have led to self–amplification of locally increased Li deposition activity, promoting further height differentiation between individual regions on the sample surface.

Figure 5 shows that deposition at increased J generally led to lower Li deposit heights on flat substrate. This was due to the above–mentioned transition from islands–like to stripe–like Li deposition patterns at rising J, causing a more spread–out and less dense deposition at high current density. As a result, less Li was concentrated in individual spots, reducing the overall deposit height. Therefore, the tallest Li structures were typically generated by deposition of high Q at low J due to the pronounced island–like Li morphology.

Regardless of the applied J, the deposits commonly exhibited a flat–topped plateau–like appearance. This was attributed to the separator that represents a physical barrier, constraining Li height growth due to the vertical pressure inside the coin cell. [30] Accordingly, formation of narrow vertical Li protrusions was suppressed in the given cell set–up. Despite the flat–topped nature of the deposits, the islands overall can still be approximated as hemispheres because there was no preferred direction of growth.

The hemispherical growth model which was discussed in Section 2.5.1 predicts a transition from hemispherically growing separated nucleation centers to overlapping growth. The initial hemispherical growth height is characterized by an exponent of $h \propto Q^{\frac{1}{3}}$. When the substrate is fully covered by deposited material, only one growth direction exists for further deposition. This leads to linear growth of the island height. The same transition was also discernible in the island height data shown in Figure 6 which was derived from LSM measurements and the transition will be supported by numerical simulations in Section 3.3 as well. This transition indicates that above $Q = 0.5$ mAhcm^2 the substrate is covered nearly completely which causes linear growth $h \propto Q$. The surface coverage in Figure 3c shows deviations from the hemispherical growth in the same region of high surface coverage.

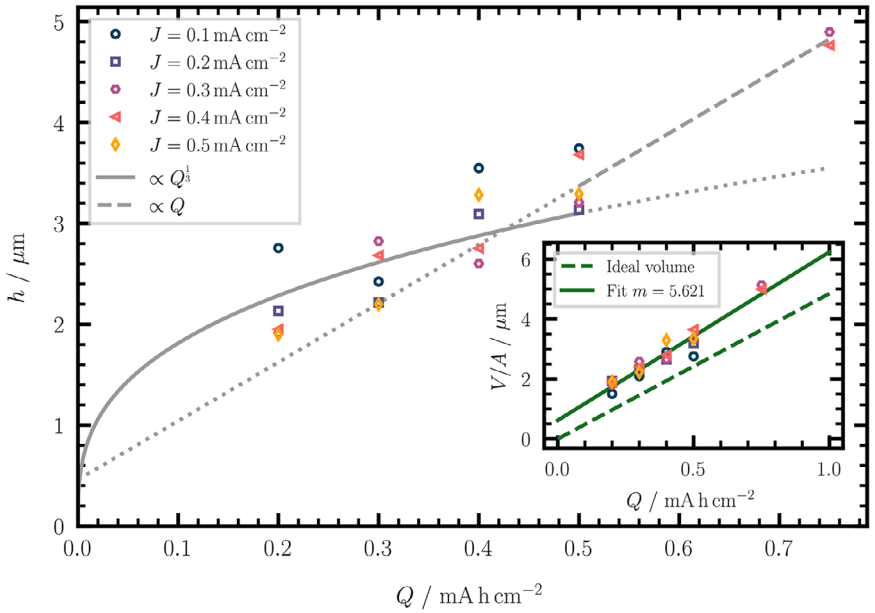

FIGURE 6 | Island height h as a function of amount of deposited material Q. Expected exponents from modeling are indicated by gray lines as a guide to the eye. According to the hemispherical model, individual islands would grow in height according to $h \propto Q^{\frac{1}{3}}$ (solid, gray line). When all nuclei have coalesced and a unified growth front is formed, the height would grow linearly with Q (dashed, gray line). Model curves outside the applicable range of Q–values are shown as dotted lines. Volume per area V/A extracted from the LSM measurements (inset). A linear fit (solid) and the ideal linear increase (dashed) of the deposited volume are indicated in green. The porosity was calculated by comparing the slope of the fit to the ideal slope. The h–offset of the fit could be explained by the surface roughness of the Cu substrate. The ideal deposited volume is calculated assuming a volume of ideally dense, non–porous Li metal equivalent to the amount of charge Q transmitted for deposition.

In addition, a weak dependency of the deposition height on the current density J could be observed for the island like growth. For small amounts of deposited material at $Q = 0.2\,\mathrm{mAhcm^2}$, separated islands were observed which became smaller and more numerous at higher J. Naturally, the average island height h in Figure 6 decreased with increasing current density J for $Q = 0.2\,\mathrm{mAhcm^2}$. For larger values of Q, the deposits became more overlapping and spatial variations on a larger scale appeared as discussed above. This eliminated the previously observed dependency of the island height on J.

The experimental LSM data allowed the calculation of the deposited volume or the average deposition height, respectively. The porosity of the deposits can be gauged by comparing the data derived from LSM to the ideal density of non–porous Li metal (cf. Section S6). The average deposition height shown in Figure 6 (inset) increased linearly with deposition amount Q. The vertical intercept can be interpreted as a systematic shift in the height data. Most likely, this was caused by the roughness of the Cu substrate which was in the order of approximately one micro meter (cf. substrate background in Figure 5 for small J). The slope of the trend line indicates the average material density. A higher slope indicates higher internal porosity. The measurements showed an internal void fraction of around 14 % compared to the ideal density of non–porous Li (cf. Section S6). No discernible dependence on the current density J was observed.

For comparison, Figure 7 shows LSM images of Li deposits on dendritic Cu foil obtained using current densities between 0.1 and 1.0 $\mathrm{mAcm^2}$ to electrodeposit the same Li amounts as discussed above for the flat substrate. To promote comparability, Figures 5 and 7 employ the same color scale to denote Li deposit height. The height maps in Figure 7 reveal that Li deposition on the rough Cu substrate regularly produced notably taller Li structures compared to flat Cu foil. This was due to the denser, more concentrated island–like morphology that dominated Li deposition on dendritic Cu foil, fostering vertical growth instead of lateral expansion of Li structures. Nevertheless, the impact of current parameter variations on the Li structure height was found to be comparable for both deposition substrates, as deposition on dendritic Cu foil analogously produced taller Li deposits at higher Q. While the deposit height was also reduced at growing J in analogy to flat Cu foil, this was due to the formation of more numerous but smaller Li islands on the dendritic substrate without transition to a stripe–like deposition pattern. The tallest Li structures were formed by deposition of high Q at low J regardless of the substrate surface roughness, highlighting this correlation as a general rule for Li deposition on Cu surfaces.

3.3 | Interpretation

To gain a mechanistic understanding of the deposition behavior, the data presented in the previous sections was augmented by insights from the numerical model introduced in Section 2.5.3.

First, Figure S10 (bottom) illustrates two distinct growth regimes as a function of sphere radius r: $V_{\mathrm{eff}} \propto r^3$ for small r, and a linear volume growth for large r. A gradual transition between these regimes emerges in the model, which can be followed by tracking the effective volume V_{eff} or Q respectively (following the equivalency of Equation (8)) with respect to the sphere radius r.

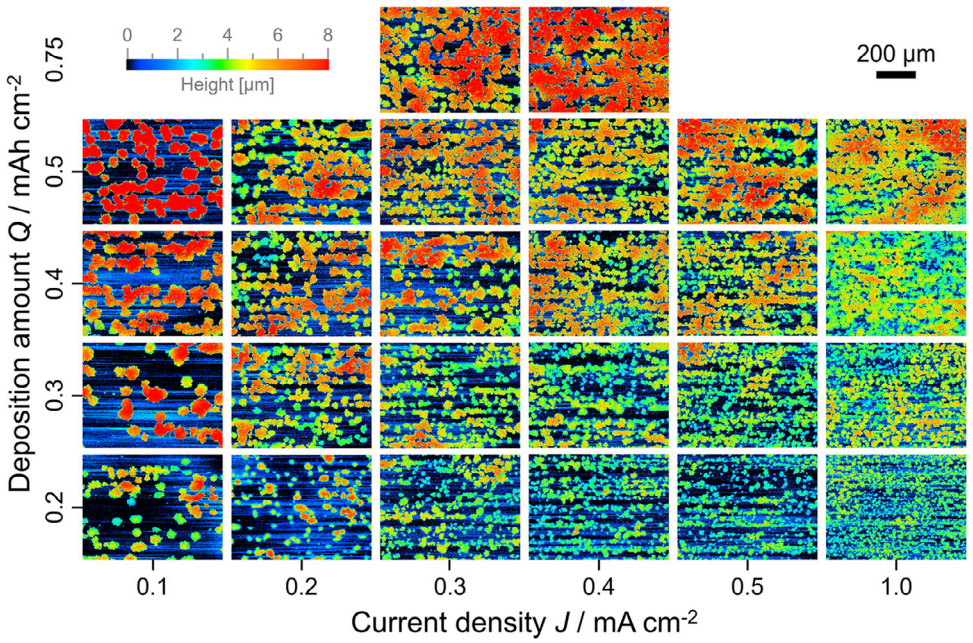

FIGURE 7 | Height maps of Li structures representing deposition amounts Q from 0.2 to 0.75 mAhcm^2 electrodeposited onto dendritic Cu foil using current density values J ranging from 0.1 to 1.0 mAcm^2. LSM images acquired using 20× lens magnification.

Initially, for small r the amount of deposited material is $Q \propto r^3$ because no overlap is present. The onset of overlap decreases the incremental rate of the effective volume increase, causing a deviation from $Q \propto r^3$ to smaller exponents. For large spheres $r \to \infty$ the effective volume depends linearly on the radius because a unified growth front has emerged growing in one dimension only (see also schematic depiction in Figure S3 (bottom)). The linear growth regime begins to start when the surface coverage is close to complete (cf. Figure S10 (top)). The transition region between these two distinct regimes exhibits a smooth transition of the exponent from $Q \propto r^3$ to $Q \propto r^1$. Numerical modeling indicates that this transition region is always centered around an exponent of two due to the symmetry of the transition. Therefore, the transition can be approximated by an effective dependence of $Q \propto r^2$. This is the relevant description for situations where the surface is not yet covered completely but neighboring islands overlap significantly.

Notably, the surface coverage shown in Figure S10 (top) exhibited maximal variance in this transition region. One realization is instantiated by positioning the spheres randomly on the surface. In the limiting case of small spheres, there is more free area than already occupied area. When placing a sphere randomly, there is only a small probability of overlap and a new sphere contributes its whole extended surface area to the total. In the other limiting case of large spheres, the whole surface is already covered. A new sphere does not contribute any newly covered area in this case. In the intermediate case, a randomly placed sphere may have any amount of overlap with its neighbors. Therefore, the variance between different realizations as well as the spatial variance is maximal.

Next, in order to trace the surface coverage $\varphi(Q)$ depending on the amount of deposited material Q with the Avrami equation (5), an expression for $S(Q)$ is needed. The extended surface coverage S in Equation (6) is $S(r) \propto r^2$ regardless of circumstances. Naturally, the resulting dependence for the relation between the extended surface coverage S and the deposited amount Q is $S(Q) \propto Q^n$. Using Equation (10), an Avrami exponent of $n = \frac{2}{3}$ is characteristic for the first growth regime which is absent of overlap. The transition region could be characterized by an effective exponent $n = 1$. In principle, the second growth regime results in $n = 2$, but this region plays no role in the discussion of the surface coverage because the surface is already covered completely. The validity of these exponents is checked by fitting the model data in Figure S11, showing that the Avrami exponent $n = 1$ describes the surface coverage best over the whole experimentally observed interval. Geometric arguments derived from superimposing the numerical data by scaling as described in Section S2.6.2 lead to an Avrami exponent $n = 1$ as well. These factors both highlight the universal applicability of the exponent $n = 1$ in the transition regime which is explored in the experiments.

Lastly, the effect of higher nucleation density is explored in Figure S12. As expected, a higher nucleation density causes a quicker convergence to full coverage for the same amount of deposited material. Interestingly, a local maximum of the variance is also observed in the simple model of overlapping hemispheres (see discussion in Section S2.4). This indicates that the experimentally observed increase of variance for a medium current density J (which directly influences the nucleation density) can be explained by simple geometric arguments only and is not necessarily a product of the complex electrochemical interplay during deposition.

The experimental measurements of the surface coverage are best described by an Avrami model with exponent $n = 1$. The hemispherical model is only able to capture the surface coverage

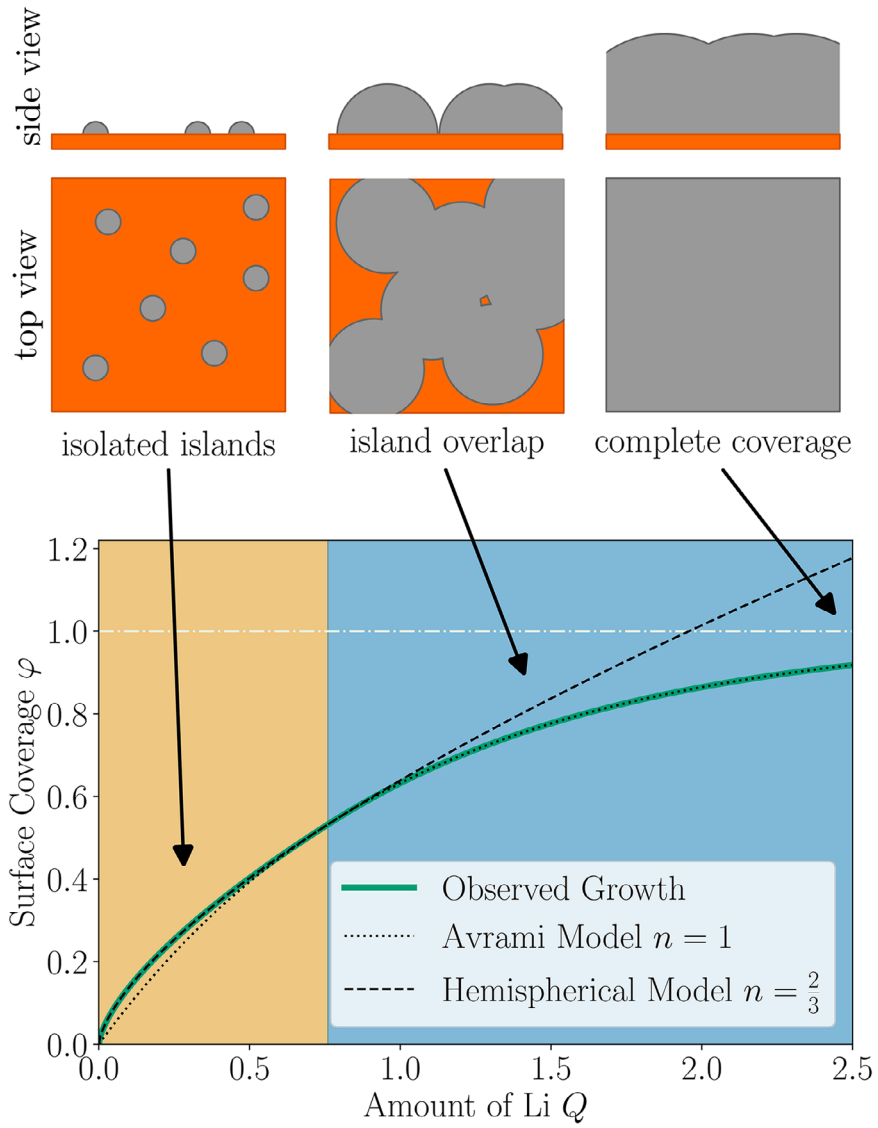

FIGURE 8 | Schematic depiction of proposed growth mechanism for Li deposition on a Cu substrate surface. The nucleation sites are formed by instantaneous nucleation from which individual islands grow without contacting each other. The fraction of covered surface φ in this stage is described exactly by the hemispherical model. The Avrami model, which incorporates overlap at all stages, describes the observed growth only approximately. After additional deposition Q, neighboring islands start to coalesce. From the point of coalescence on, the surface coverage is captured well by the Avrami exponent $n = 1$, but the hemispherical model starts to deviate. This distinction between separated and overlapping islands is indicated by the change of background color in the graph. When the substrate is covered completely, a unified growth front emerges. The hemispherical model would predict physically implausible high surface coverage values of $\varphi > 1$, whereas the Avrami model captures the convergence to complete surface coverage.

in a region of $\varphi < 85\%$. This indicates that the deposits do not overlap significantly in this region, but overlap becomes significant for higher coverage. In combination with the numerical simulations, a unified mechanism for the electrodeposition of Li on flat Cu substrate can be deducted and is depicted in Figure 8. After an instantaneous nucleation of the initial Li deposits, individual islands grow separately. Later, neighboring islands start to coalesce and cover the substrate completely.

During the intermediate stage between island growth and complete surface coverage, the experimental SEM data showed a peak in variance of the surface coverage. The same anomaly has been observed and reasoned about in the numerical model. It may be possible that in the experiment additional variance was caused by non–uniform nucleation due to heterogeneous current density.

Analogously, the height evolution of the deposits observed experimentally by LSM can also be understood by comparing to the numerical model. The height grows initially with $h \propto t^{\frac{1}{3}}$ in the first growth regime. After some time, the islands coalesce to a unified growth front in the second growth regime. Here, the deposition height increases linearly with Q. The transition indicated by the experimental LSM data is compatible with the proposed growth mechanism in Figure 8.

4 | Conclusion

In this article, the combination of experimental imaging techniques and a simple computer model was used to phenomenologically capture the deposition mechanism of lithium on copper

substrates. The accompanying model proved indispensable for interpreting the corresponding experimental phenomena, especially in regimes where nuclei overlapped. Li structures generated by electrodeposition at current densities J from 0.1 to 1.0 mAcm^2 with deposition amounts Q from 0.2 to 0.75 mAhcm^2 were characterized by SEM and LSM measurements. Naturally, higher deposition amounts Q caused more of the planar Cu substrate surface to be covered with Li. Nucleation sites were created instantaneously upon applying the charging current, and the surface coverage could be described by hemispheres of equal size growing independently on the surface initially. In this growth phase, the hemispherical growth model with a geometrical exponent of $\frac{2}{3}$ was sufficient to describe the observed substrate coverage. When the deposition amount Q was increased, the experimentally observed Li structures expanded laterally and started to coalesce. At this point, when overlap of neighboring islands started to occur, the simple hemispherical model was no longer able to describe the observed surface coverage. During this growth phase, an Avrami model with an Avrami exponent of $n = 1$ was suitable to describe the experimental observations. Further analysis of the model revealed the general applicability of an Avrami exponent $n = 1$ for coalescing nuclei. Concretely, computer simulations showed that this effective exponent was the result of a universally observed exponent of the deposition volume which enters the Avrami equation. This argument applies to various contact angles and non–spherical geometries, as long as growth has no preferred direction. Analogously, the Li deposit height increased with rising Q, as observed by LSM. This increase initially progressed according to the hemispherical model with an exponent of $\frac{1}{3}$. When islands coalesced, a transition toward complete surface coverage and film growth was observed which was described by linear growth. This model was able to describe the experimental observations and the exact transition could be resolved by computer simulations.

Rising current densities J increased the surface coverage for small amounts of deposited material because a larger number of nucleation sites were formed, increasing the nucleation density. For large Li deposition amounts Q, the surface coverage was found to be nearly complete irrespective of current density. In between these two extremes, at medium deposition amounts Q, a large scale spatial heterogeneity was observed for a critical current density. This critical current density was located at the transition point between partial and full substrate coverage. Although reproducible by modeling, the mechanisms underpinning the critical current density are not yet fully elucidated. One contribution to this variance effect could be found in the inherent variance of overlap when randomly arranging deposition islands of varying size and number in modeling. Also, the exact value of the critical current density may depend on experimental parameters such as the employed electrolyte composition. Furthermore, the microscopic deposition structure became less smooth for higher current densities, but no significant change in internal porosity was observed within measurement accuracy.

Generally, the Li deposits were found to align to the surface structure of the substrate more strongly with rising current density J. Although, even the island growth which was observed for smaller current densities followed distinct lines on the substrate surface structure. When transitioning from individual islands to complete surface coverage at high J, elevated regions of the grooved surface structure of the planar Cu substrate were found to be preferred for deposition due to local Li diffusion kinetics. Dendritic Cu foil was employed as a comparison to the slightly textured planar substrate. Here, no coalescence of the individual islands was observed over a wide range of deposition amounts and current densities due to the higher lithiophobicity of the substrate.

Author Contributions

Co–first authors are T. Ingber and L. Kimms. Experimental data acquisition has been performed by T. Ingber and model development and analysis were done by L. Kimms. Analysis of the experimental data and discussion within the results section were done conjointly by the first authors. The introduction and experimental sections were authored predominantly by T. Ingber. The remaining methodology, interpretation, and conclusion sections were authored for the largest part by L. Kimms. M. Winter acquired funding for experimental resources, provided institutional support for the experiments, and reviewed the manuscript. A. Heuer and D. Diddens supervised the project and reviewed the manuscript.

Acknowledgements

We thank Marian Stan for helpful ideas and thoughtful discussions. This work was supported by the German Federal Ministry of Education and Research (BMBF) within MEET Hi–EnD III (03XP0258A).

Open access funding enabled and organized by Projekt DEAL.

Conflicts of Interest

The authors declare no conflicts of interest.

Data Availability Statement

The data that support the findings of this study as well as the software used for modeling are provided via Zenodo: https://doi.org/10.5281/zenodo.17828430.

References

1. M. Winter, B. Barnett, and K. Xu, "Before Li Ion Batteries," *Chemical Reviews* 118, no. 23 (2018): 11433–11456.

2. T. Placke, R. Kloepsch, S. Dühnen, and M. Winter, "Lithium Ion, Lithium Metal, and Alternative Rechargeable Battery Technologies: The Odyssey for High Energy Density," *Journal of Solid State Electrochemistry* 21, no. 7 (2017): 1939–1964.

3. G. M. Hobold, J. Lopez, R. Guo, et al., "Moving Beyond 99.9% Coulombic Efficiency for Lithium Anodes in Liquid Electrolytes," *Nature Energy* 6, no. 10 (2021): 951–960.

4. Y. Zhang, T.-T. Zuo, J. Popovic, et al., "Towards Better Li Metal Anodes: Challenges and Strategies," *Materials Today* 33 (2020): 56–74.

5. J.-G. Zhang, W. Xu, J. Xiao, X. Cao, and J. Liu, "Lithium Metal Anodes with Nonaqueous Electrolytes," *Chemical Reviews* 120, no. 24 (2020): 13 312–13 348.

6. X. He, D. Bresser, S. Passerini, et al., "The Passivity of Lithium Electrodes in Liquid Electrolytes for Secondary Batteries," *Nature Reviews Materials* 6, no. 11 (2021): 1036–1052.

7. C. Heubner, S. Maletti, H. Auer, et al., "From Lithium-Metal Toward Anode-Free Solid-State Batteries: Current Developments, Issues, and Challenges," *Advanced Functional Materials* 31, no. 51 (2021): 2106608.

8. J. T. Frith, M. J. Lacey, and U. Ulissi, "A Non-Academic Perspective on the Future of Lithium-Based Batteries," *Nature Communications* 14, no. 1 (2023): 420.

9. T. T. K. Ingber, M. M. Bela, F. Püttmann, et al., "Elucidating the Lithium Deposition Behavior in Open-Porous Copper Micro-Foam Negative Electrodes for Zero-Excess Lithium Metal Batteries," *Journal of Materials Chemistry A* 11, no. 33 (2023): 17828–17840.

10. O. Lohrberg, S. Maletti, C. Heubner, M. Schneider, and A. Michaelis, "Understanding Li Plating and Stripping Behavior in Zero-Excess Li Metal Batteries Using Operando Dilatometry," *Journal of The Electrochemical Society* 169, no. 3 (2022): 030543.

11. Z. Xie, Z. Wu, X. An, et al., "Anode-Free Rechargeable Lithium Metal Batteries: Progress and Prospects," *Energy Storage Materials* 32 (2020): 386–401.

12. E. Kazyak, M. J. Wang, K. Lee, et al., "Understanding the Electro-Chemo-Mechanics of Li Plating in Anode-Free Solid-State Batteries with Operando 3D Microscopy," *Matter* 5, no. 11 (2022): 3912–3934.

13. M. Genovese, A. J. Louli, R. Weber, R. J. Sanderson, M. B. Johnson, and J. R. Dahn, "Combinatorial Methods for Improving Lithium Metal Cycling Efficiency," *Journal of The Electrochemical Society* 165, no. 13 (2018): A3000–A3013.

14. B. J. Neudecker, N. J. Dudney, and J. B. Bates, ""Lithium-Free" Thin-Film Battery with In Situ Plated Li Anode," *Journal of The Electrochemical Society* 147, no. 2 (2000): 517.

15. S. Stuckenberg, M. M. Bela, C. Lechtenfeld, et al., "Influence of $LiNO_3$ on the Lithium Metal Deposition Behavior in Carbonate-Based Liquid Electrolytes and on the Electrochemical Performance in Zero-Excess Lithium Metal Batteries," *Small* 20, no. 6 (2024): 2305203.

16. V. Pande and V. Viswanathan, "Computational Screening of Current Collectors for Enabling Anode-Free Lithium Metal Batteries," *ACS Energy Letters* 4, no. 12 (2019): 2952–2959.

17. Q. Shi, C. Lu, Y. Cao, et al., "Recent Developments in Current Collectors for Lithium Metal Anodes," *Materials Chemistry Frontiers* 7, no. 7 (2023): 1298–1311.

18. B. Zhou, A. Bonakdarpour, I. Stoševski, B. Fang, and D. P. Wilkinson, "Modification of Cu Current Collectors for Lithium Metal Batteries – A Review," *Progress in Materials Science* 130 (2022): 100996.

19. C.-J. Huang, B. Thirumalraj, H.-C. Tao, et al., "Decoupling the Origins of Irreversible Coulombic Efficiency in Anode-Free Lithium Metal Batteries," *Nature Communications* 12, no. 1 (2021): 1452.

20. M. R. Cosby, G. M. Carignan, Z. Li, et al., "Operando Synchrotron Studies of Inhomogeneity during Anode-Free Plating of Li Metal in Pouch Cell Batteries," *Journal of The Electrochemical Society* 169, no. 2 (2022): 020571.

21. Z. Tong, B. Bazri, S.-F. Hu, and R.-S. Liu, "Interfacial Chemistry in Anode-Free Batteries: Challenges and Strategies," *Journal of Materials Chemistry A* 9, no. 12 (2021): 7396–7406.

22. K. Dong, Y. Xu, J. Tan, et al., "Unravelling the Mechanism of Lithium Nucleation and Growth and the Interaction with the Solid Electrolyte Interface," *ACS Energy Letters* 6, no. 5 (2021): 1719–1728.

23. L. Frenck, G. K. Sethi, J. A. Maslyn, and N. P. Balsara, "Factors That Control the Formation of Dendrites and Other Morphologies on Lithium Metal Anodes," *Frontiers in Energy Research* 7 (2019): 115.

24. S. Menkin, C. A. O'Keefe, A. B. Gunnarsdóttir, et al., "Toward an Understanding of SEI Formation and Lithium Plating on Copper in Anode-Free Batteries," *The Journal of Physical Chemistry C* 125, no. 30 (2021): 16 719–16 732.

25. X. Wang, G. Pawar, Y. Li, et al., "Glassy Li Metal Anode for High-Performance Rechargeable Li Batteries," *Nature Materials* 19, no. 12 (2020): 1339–1345.

26. B. Liaw, G. Pawar, Y. S. Meng, C. Fang, and B. Lu, "Perspective–Lithium Metal Nucleation and Growth on Conductive Substrates: A Multi-Scale Understanding from Atomistic, Nano-, Meso-, to Micro-Scales," *Journal of The Electrochemical Society* 169, no. 11 (2022): 112505.

27. H. Kühnle, E. Knobbe, and E. Figgemeier, "In Situ Optical Investigations of Lithium Depositions on Pristine and Aged Lithium Metal Electrodes," *Journal of The Electrochemical Society* 168, no. 2 (2021): 020510.

28. M. Romio, J. Kahr, E. Miele, et al., "*Operando* Optical Microscopy of Dead Lithium Growth in Anode-Less Configuration," *Advanced Materials Technologies* 9, no. 13 (2024): 2301902.

29. H. Kühnle, S. Berg, S. Frese, E. Knobbe, and E. Figgemeier, "Image-Based Quantification of Deposited Lithium on Li Metal Surfaces," *Energy Technology* 13 (2025): 2500364.

30. J. Sun, J. Peng, T. Ring, et al., "Lithium Deposition Mechanism on Si and Cu Substrates in the Carbonate Electrolyte," *Energy and Environmental Science* 15, no. 12 (2022): 5284–5299.

31. R. Weber, M. Genovese, A. J. Louli, et al., "Long Cycle Life and Dendrite-Free Lithium Morphology in Anode-Free Lithium Pouch Cells Enabled by a Dual-Salt Liquid Electrolyte," *Nature Energy* 4, no. 8 (2019): 683–689.

32. A. J. Louli, M. Genovese, R. Weber, S. G. Hames, E. R. Logan, and J. R. Dahn, "Exploring the Impact of Mechanical Pressure on the Performance of Anode-Free Lithium Metal Cells," *Journal of The Electrochemical Society* 166, no. 8 (2019): A1291–A1299.

33. C. Zhou, A. J. Samson, M. A. Garakani, and V. Thangadurai, "Communication–Anode-Free Lithium Metal Batteries: A Case Study of Compression Effects on Coin Cell Performance," *Journal of The Electrochemical Society* 168, no. 6 (2021): 060532.

34. M. Avrami, "Kinetics of Phase Change. I General Theory," *The Journal of Chemical Physics* 7, no. 12 (1939): 1103–1112.

35. M. Avrami, "Kinetics of Phase Change. II Transformation-Time Relations for Random Distribution of Nuclei," *The Journal of Chemical Physics* 8, no. 2 (1940): 212–224.

36. G. Lai, J. Jiao, C. Fang, et al., "The Mechanism of Li Deposition on the Cu Substrates in the Anode-Free Li Metal Batteries," *Small* 19, no. 3 (2023): 2205416.

37. T. Jang, J.-H. Kang, S. Kim, et al., "Nanometer-Scale Surface Roughness of a 3-D Cu Substrate Promoting Li Nucleation in Li-Metal Batteries," *ACS Applied Energy Materials* 4, no. 3 (2021): 2644–2651.

38. N. Otsu, "A Threshold Selection Method from Gray-Level Histograms," *IEEE transactions on systems, man, and cybernetics* 9, no. 1 (1979): 62–66.

39. A. Chambolle, "An Algorithm for Total Variation Minimization and Applications," *Journal of Mathematical Imaging and Vision* 20, no. 1/2 (2004): 89–97.

40. K. B. Shaik, P. Ganesan, V. Kalist, B. Sathish, and J. M. M. Jenitha, "Comparative Study of Skin Color Detection and Segmentation in HSV and YCbCr Color Space," *Procedia Computer Science* 57 (2015): 41–48.

41. M. Fanfoni and M. Tomellini, "The Johnson-Mehl-Avrami-Kohnogorov Model: A Brief Review," *Il Nuovo Cimento D* 20, no. 7–8 (1998): 1171–1182.

42. L. Guo, G. Oskam, A. Radisic, P. M. Hoffmann, and P. C. Searson, "Island Growth in Electrodeposition," *Journal of Physics D: Applied Physics* 44, no. 44 (2011): 443001.

43. K. Shirzad and C. Viney, "A Critical Review on Applications of the Avrami Equation Beyond Materials Science," *Journal of The Royal Society Interface* 20, no. 203 (2023): 20230242.

44. A. Pei, G. Zheng, F. Shi, Y. Li, and Y. Cui, "Nanoscale Nucleation and Growth of Electrodeposited Lithium Metal," *Nano Letters* 17, no. 2 (2017): 1132–1139.

45. M. E. Hyde and R. G. Compton, "A Review of the Analysis of Multiple Nucleation with Diffusion Controlled Growth," *Journal of Electroanalytical Chemistry* 549 (2003): 1–12.

46. W. Wang, Z. Li, S. Chen, et al., "The Overlooked Role of Copper Surface Texture in Electrodeposition of Lithium Revealed by Electron Backscatter Diffraction," *ACS Energy Letters* 9, no. 1 (2024): 168–175.

47. K. Chen, R. Pathak, A. Gurung, et al., "A Copper-Clad Lithiophilic Current Collector for Dendrite-Free Lithium Metal Anodes," *Journal of Materials Chemistry A* 8, no. 4 (2020): 1911–1919.

48. C. Wang, M. Liu, M. Thijs, F. G. B. Ooms, S. Ganapathy, and M. Wagemaker, "High Dielectric Barium Titanate Porous Scaffold for Efficient Li Metal Cycling in Anode-Free Cells," *Nature Communications* 12, no. 1 (2021): 6536.

49. C.-P. Yang, Y.-X. Yin, S.-F. Zhang, N.-W. Li, and Y.-G. Guo, "Accommodating Lithium into 3D Current Collectors with a Submicron Skeleton Towards Long-Life Lithium Metal Anodes," *Nature Communications* 6, no. 1 (2015): 8058.

Supporting Information

Additional supporting information can be found online in the Supporting Information section.

Supporting File: admi70470-sup-0001-SuppMat.pdf.